ADVANCES IN ATMOSPHERIC SCIENCES, VOL. 41, OCTOBER 2024, 1953–1968

• **Original Paper** •

Retrieval of Volcanic Sulfate Aerosols Optical Parameters from AHI Radiometer Data

Andrei FILEI*[1], Olga GIRINA[2], and Aleksei SOROKIN[3]

[1]*Far-Eastern Center of State Research Center for Space Hydrometeorology «Planeta»*, *Khabarovsk* 680000, *Russia*

[2]*Institute of Volcanology and Seismology Far Eastern Branch of the Russian Academy of Sciences*, *Petropavlovsk-Kamchatsky* 683006, *Russia*

[3]*Computing Center of the Far Eastern Branch of the Russian Academy of Sciences*, *Khabarovsk* 680000, *Russia*

(Received 23 May 2023; revised 12 March 2024; accepted 28 March 2024)

ABSTRACT

This paper presents a method for retrieving optical parameters from volcanic sulfate aerosols from the AHI radiometer on board the Himawari-8 satellite. The proposed method is based on optical models for various mixtures of aerosol components from volcanic clouds, including ash particles, ice crystals, water drops, and sulfate aerosol droplets. The application of multi-component optical models of various aerosol compositions allows for the optical thickness and mass loading of sulfate aerosol to be estimated in the sulfuric cloud formed after the Karymsky volcano eruption on 3 November 2021. A comprehensive analysis of the brightness temperatures of the sulfuric cloud in the infrared bands was performed, which revealed that the cloud was composed of a mixture of sulfate aerosol and water droplets. Using models of various aerosol compositions allows for the satellite-based estimation of optical parameters not only for sulfate aerosol but also for the whole aerosol mixture.

Key words: H_2SO_4, volcano, Himawari-8, mass loading, volcanic ash, optical thickness, the Karymsky volcano

Citation: Filei, A., O. Girina, and A. Sorokin, 2024: Retrieval of volcanic sulfate aerosols optical parameters from AHI radiometer data. *Adv. Atmos. Sci.*, **41**(10), 1953−1968, https://doi.org/10.1007/s00376-024-3105-2.

Article Highlights:

- A method for retrieving the optical parameters of volcanic sulfuric acid from the AHI sensor on board Himawari-8 is presented.
- The optical models for different mixtures of volcanic cloud aerosol components were used for the retrieval of optical thickness and mass loading of sulfate aerosol.
- It is demonstrated that the use of models with various aerosol compositions allows for the estimation of the optical parameters for any aerosol mixture.

1. Introduction

Volcanic eruptions are the source of inflow of ash, aerosol particles, and trace gases into the atmosphere. In general, volcanic clouds consist of ash particles, water vapor (H_2O), sulfur dioxide (SO_2), and aqueous solutions of sulfuric acid (SA). Upon reaching the upper atmospheric layers, volcanic clouds can move large distances from volcanoes over the timescale of weeks or even a few years, reducing solar radiation intensity (Girina et al., 2022). The transport of high concentrations of volcanic ash and gases can harm human health and damage ecosystems near volcanoes; however, it can also have much broader-scale consequences, including threatening air traffic and impacting global climate (McCormick et al., 1995; Miller and Casadevall, 2000; Prata and Rose, 2015). For example, the impacts associated with the eruptions of Icelandic volcanoes in 2010 and 2011 (Ulfarsson and Unger, 2011), as well as the strongest eruption of Hunga Tonga–Hunga Ha'apai volcano in the last 30 years on 14 January 2022 (Bennis and Venzke, 2022), highlight that operational monitoring of active volcanoes is essential to determine the threat that they pose.

Satellite-based remote sensing data have been widely used to detect volcanic clouds and determine their optical and microphysical characteristics. The radiometers on board satellites can be used to provide information about volcanic cloud characteristics in various spectral bands. Since the late 1980s, methods using infrared (IR) (Prata, 1989) and ultraviolet (UV) (Eisinger and Burrows, 1998) radiation

* Corresponding author: Andrei FILEI
Email: vmer@dvrcpod.ru

have been used to detect volcanic ash and SO_2. The modern approaches for determining the parameters (e.g., cloud altitude, mass loading, optical thickness) of volcanic ash and SO_2 are presented in (e.g., Ishii et al., 2018; Hedelt et al., 2019; Filei and Marenco, 2021; Piontek et al., 2021; Bugliaro et al., 2022; Koukouli et al., 2022; Li et al., 2022; Theys et al., 2023). In the 1990s, techniques for detecting SA were developed for data from the HIRS/2 IR hyperspectrometer on board the NOAA satellites (Ackerman and Strabala, 1994) and from the MODIS radiometer in IR bands at the wavelengths of 8.5, 11, and 12 μm (Ackerman, 1997). Currently, IR hyperspectrometers are the most common approach used to detect SA and retrieve its parameters (Karagulian et al., 2010; Sellitto and Legras, 2016; Sellitto et al., 2023). Recent achievements in SA parameter retrieval using low-resolution passive spectrometers are presented in (Sellitto and Legras, 2016; Guermazi et al., 2017; Sellitto et al., 2017). Given that passive satellite sensors (e.g., VIIRS, AHI, SEVIRI) are installed on most modern hydrometeorological satellites, using these sensors to characterize the parameters of volcanic aerosol (in particular SA) allows volcanologists to evaluate the risks associated with a volcanic eruption. The existing methods for determining the SA parameters are based on the "classic scheme" within which the volcanic cloud is considered a single-component aerosol: liquid/ice cloud, volcanic ash, or SA. However, the technique presented in this paper simultaneously characterizes various mixtures of aerosol components of volcanic clouds, consisting of ash of various types (andesite or basalt) along with drops of water or an aqueous solution of SA. This technique allows for a satellite-based estimation of optical parameters not only for SA but also for the entire aerosol mixture.

This study develops a new technique for retrieving volcanic SA optical parameters from the AHI radiometer on board the Himawari-8 geostationary satellite (hereafter referred to as Himawari-8/AHI). This method is based on using optical models for different mixtures of the volcanic cloud's aerosol components represented by ash particles, ice crystals, water drops, and sulfate aerosol droplets. The multicomponent optical models of the various aerosol compositions for estimating the optical thickness and mass loading of SA in a sulfuric cloud are demonstrated for a case study of the Karymsky volcano eruption on 3 November 2021.

The remainder of this paper is organized as follows. Section 2 presents details on the optical models used in this study. Section 3 investigates the gaseous components of volcanic clouds, while section 4 focuses on the remotely sensed SA retrieval process. Section 5 investigates the optimal method retrieval process. Section 6 presents the results and discussion and finally, section 7 summarizes the study.

2. Optical models of volcanic clouds

Volcanic clouds comprise a mixture of different components that can include ash particles, water drops, ice crystals, and sulfate aerosol droplets. Droplets of sulfate aerosol in aqueous solution are always present in volcanic clouds; however, their percentage in such clouds varies depending on the eruption character. Typical volcanic clouds contain aqueous solutions of 75% H_2SO_4 and 25% H_2O (liquid droplets) that have long lifetimes in the atmosphere: in the troposphere, these can last for several days or weeks, while in the stratosphere, they can last for several months or even years (Guermazi et al., 2017). It is worth noting that SA in the proportion of 75/25% represents an average value in a volcanic cloud, and its proportion can vary depending on the aerosol composition of the volcanic cloud, the temperature, and the pressure of the atmospheric layer on which this volcanic cloud is located. According to Ohtake (1993), sulfate aerosol droplets have different freezing points depending on the air pressure and the concentration of SA in the aqueous solution. For example, 75% of SA solutions freeze at a temperature of –100°C, and the frozen droplets have a morphology similar to that of ice crystals. Given their low freezing point, volcanic SA particles most often occur in the atmosphere as liquid droplets.

The interaction of electromagnetic radiation with the volcanic cloud components depends on the ratio of the particle size, particle shape, and wavelength. The real component of the refractive index describes the refraction of light incident on the particle, while the imaginary component indicates absorption. Figure 1 illustrates the dependence of the imaginary component (n_i) of the complex refractive index of volcanic cloud components on wavelength.

Data on n_i values for andesite were taken from Pollack et al. (1973), data for SA were taken from Remsberg et al. (1974), and data for water and ice particles were taken from Hale and Querry (1973) and Warren (1984), respectively. Ash from most volcanoes in the world is typically represented by glass particles of dacitic, andesitic, basaltic, and basaltic andesite composition. The complex refractive indices of andesite and basalt rocks are similar; accordingly, the volcanic ash in this study was assumed to have the properties of andesite, especially given that rocks of the Karymsky volcano have primarily andesitic compositions. Spectral bands with wavelengths of 11 and 12 μm are known to be suitable for detecting volcanic ash in satellite images and retrieving its parameters (Prata, 1989; Wen and Rose, 1994). As shown in Fig. 1, IR radiation absorption of the ash particles at 11 um is stronger than at 12 um, while the opposite is true of water drops and ice crystals. Since SA has similar absorption properties to ash at 11 and 12 μm wavelengths, the 8.5 μm channel is also required to identify it in satellite images. Depending on the concentration and particle size distribution, sulfate aerosol droplets may show much stronger absorption at 8.5 μm than ash and clouds. Thus, the joint use of AHI radiometer channels with central wavelengths of 8.7, 11.2, and 12.4 μm is necessary to detect SA accurately.

Assuming that the volcanic cloud is a homogeneous, plane-parallel layer, the IR radiation intensity registered by the satellite sensor at the top of the atmosphere is determined by the following expression (Pavolonis, 2010):

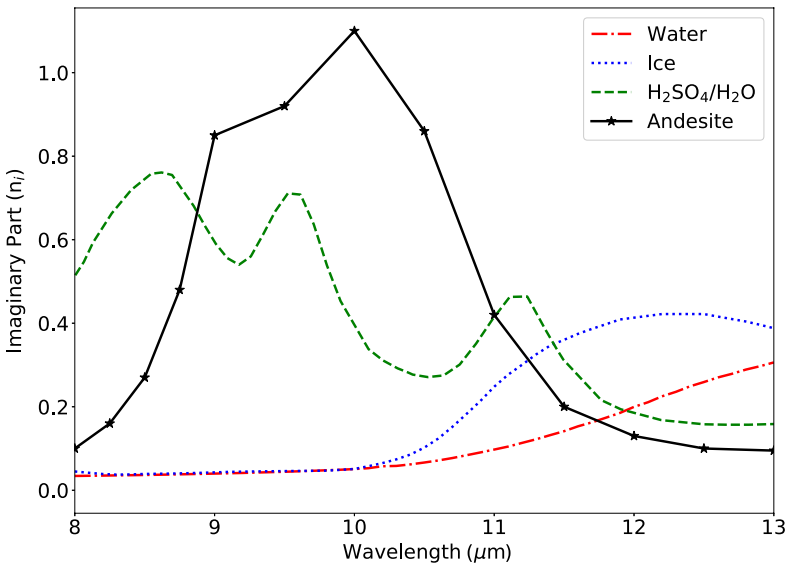

Fig. 1. The dependence of n_i on wavelength for volcanic cloud aerosol components.

$$R_{\text{obs}} = (1-\varepsilon)(R_{\text{clr}} - R_{\text{ac}}) + R_{\text{ac}} + \varepsilon t_{\text{ac}} B(T_{\text{cld}}) \,, \tag{1}$$

where R_{obs} is the IR radiation intensity at the top of the atmosphere, ε is the emissivity of the volcanic cloud, R_{clr} is the radiance of the "clear" atmosphere, R_{ac} and t_{ac} are the above-cloud upwelling atmospheric radiance and transmittance, respectively, B is the Planck function, and T_{cld} is the brightness temperature of the volcanic cloud.

Volcanic cloud emissivity ε in Eq. (1) is directly related to the microphysical parameters of the volcanic aerosol, which are determined by the optical thickness τ_{aer} with the following expression:

$$\begin{aligned} \tau_{\text{aer},\lambda} &= -\ln(1-\varepsilon_\lambda)\cos\theta \\ &= \ln\left[\frac{R_{\text{obs},\lambda} - (R_{\text{ac},\lambda} + t_{\text{ac},\lambda} B(T_{\text{cld},\lambda}))}{R_{\text{clr},\lambda} - (R_{\text{ac},\lambda} + t_{\text{ac},\lambda} B(T_{\text{cld},\lambda}))}\right], \end{aligned} \tag{2}$$

where θ is the satellite zenith angle, λ is the wavelength.

Volcanic cloud microphysical parameters cannot be captured with the cloud emissivity of one spectral channel; instead, it is the spectral variation of the volcanic cloud emissivity that holds the aerosol microphysical information. To account for this, the volcanic cloud emissivity is used to calculate optical thickness ratios, also known as β_{eff}. The coefficient β_{eff} is calculated directly from satellite measurements and is equal to the ratio of optical thicknesses τ_{aer} for a given pair of channels in the IR band, which is defined as follows:

$$\begin{aligned} \beta_{\text{eff},\lambda_1/\lambda_2} &= \frac{\tau_{\text{aer},\lambda_1}}{\tau_{\text{aer},\lambda_2}} = \frac{\ln(1-\varepsilon_{\lambda_1})}{\ln(1-\varepsilon_{\lambda_2})} \\ &= \frac{\ln\left[\dfrac{R_{\text{obs},\lambda_1} - (R_{\text{ac},\lambda_1} + t_{\text{ac},\lambda_1} B(T_{\text{cld},\lambda_1}))}{R_{\text{clr},\lambda_1} - (R_{\text{ac},\lambda_1} + t_{\text{ac},\lambda_1} B(T_{\text{cld},\lambda_1}))}\right]}{\ln\left[\dfrac{R_{\text{obs},\lambda_2} - (R_{\text{ac},\lambda_2} + t_{\text{ac},\lambda_2} B(T_{\text{cld},\lambda_2}))}{R_{\text{clr},\lambda_2} - (R_{\text{ac},\lambda_2} + t_{\text{ac},\lambda_2} B(T_{\text{cld},\lambda_2}))}\right]}. \end{aligned} \tag{3}$$

A similar ratio was used by Parol et al. (1991) to retrieve the parameters of cirrus clouds (specifically the size of the aerosol particles from AVHRR satellite instrument data), as well as in (Pavolonis et al. (2013) and Filei and Marenco, (2021) to retrieve the parameters of volcanic ash.

The coefficient β_{eff} can be interpreted in terms of the single scattering properties; it can be calculated from the extinction coefficient k_{ext}, single-scattering albedo ω, and asymmetry factor g, as follows (Parol et al., 1991):

$$\beta_{\text{theo},\lambda_1/\lambda_2} = \frac{(1-\omega_{\lambda_1} g_{\lambda_1}) k_{\text{ext},\lambda_1}}{(1-\omega_{\lambda_2} g_{\lambda_2}) k_{\text{ext},\lambda_2}} \,. \tag{4}$$

The coefficient β_{theo} represents the ratio of scaled extinction coefficients, and it can be computed for a given volcanic cloud composition and aerosol particle distribution. The coefficient β_{theo} is used to extract cloud, volcanic ash, and dust cloud microphysical information from infrared measurements (Parol al., 1991; Heidinger and Pavolonis, 2009; Pavolonis, 2010; Pavolonis et al., 2013).

Since the effects of multiple scattering in the 8–13 μm IR region are minor, β_{eff} retrieved from satellite data will be approximately equal to the model β_{theo} computed using Mie theory (Pavolonis et al., 2013):

$$\beta_{\text{eff}} \approx \beta_{\text{theo}} \,. \tag{5}$$

By using β_{eff}, we are accounting for the non-cloud contribution to the radiances, and we are also providing a means to calculate the optical and microphysical parameters of the volcanic aerosol. To calculate β_{eff}, we used three properties of the single-scatter of volcanic aerosol: k_{ext}, ω, and g. The parameters k_{ext}, ω, and g represent the basis for optical models of volcanic clouds in the current paper. Assuming that aerosol particles have a spherical form, the parameters k_{ext}, ω, and g can be computed using Mie theory by using the cor-

responding complex refractive index of aerosol and size distributions of particles. In the current study, these calculations were performed using the algorithm implemented in the libRadtran library (Mayer and Kylling, 2005). Four volcanic cloud components were considered to calculate the optical parameters: ice crystals, water drops, sulfate aerosol droplets, and andesite particles. Log-normal distributions were used for the andesite particles and SA aqueous solution droplets (Liu and Penner, 2002; Clarisse et al., 2010; Clarisse and Prata, 2016; Roberts et al., 2018), while a gamma distribution was applied to the water drops (Mayer and Kylling, 2005). Unlike the ice crystals, all other aerosol components were assumed to be spherical. The optical properties of the volumetric scattering of cloud ice crystals were taken from the scattering model presented in (Baum et al., 2005a, b).

The aerosol particle distributions in a volcanic cloud can be described in terms of their effective radius r_e, which is an area-average value of the radius of the aerosol particles. The effective radius allows the size of aerosol particles of various shapes to be described, for example, by comparing the area of these particles with the area of a spherical particle of known radius, thus generating an effective radius value. Optical models are calculated for different variations of r_e, and each model has different values of the parameters k_{ext}, ω, and g, which are dependent on the wavelength λ. Table 1 presents, as an example, the calculated optical parameters of aerosol components for the 8–13 μm spectral band. The optical models for the Mie calculations were constructed for a wide range of r_e values for the volcanic cloud aerosol components. When calculating the optical parameters, the following r_e values were considered: volcanic ash: 0.1, 0.25, 0.5, 1.0, 2.0, 3.0, 5.0, 7.0, 9.0, 11.0, 13.0, 15.0, 17.0, and 20.0 μm; water drops: 1, 3, 5, 10, 15, and 20 μm; ice crystals: 5, 10, 20, 30, 40, 50, 60, and 70 μm; sulfate aerosol droplets: 0.1, 0.2, 0.3, 0.4, 0.5, 0.6, 0.8, 1.0, 1.5, 2.0, and 3.0 μm.

According to (Ensor and Pilat, 1971), the relationship between the aerosol mass concentration of aerosol particles (W_{aer}) and k_{ext} can be expressed using the mass extinction coefficient m_{ext}:

$$m_{ext} = \frac{k_{ext}}{W_{aer}} = \frac{1}{\rho}\left[\frac{\int_{r_1}^{r_2} Q_{ext} r^2 n(r)\mathrm{d}r}{\frac{4}{3}\int_{r_1}^{r_2} r^3 n(r)\mathrm{d}r}\right], \quad (6)$$

where Q_{ext} is the extinction efficiency factor, r is the particle size, $n(r)$ is the particle size distribution function, and ρ is the particle density.

As volcanic clouds represent an external mixture of different components, this study considered not only the separate components but also mixed aerosol systems. To simplify the calculation, only binary mixtures were used. In the present work, only two-component mixtures are considered. Numerous optical models for mixtures of aerosol components with different compositions were constructed in this study. The following mixtures were considered: andesite particles and ice crystals, andesite particles and water drops, andesite particles

Table 1. The optical parameters of aerosol components.

λ, (μm)	Andesite particles r_e = 2 μm, ρ = 2.6 g cm^{-3} sz = lognormal σ = 2.1			Sulphate aerosol droplets r_e = 0.6 μm, ρ = 1.84 g cm^{-3} sz = lognormal σ = 1.86			Water drops r_e =10 μm, ρ = 1.0 g cm^{-3} sz = gamma			Ice crystals r_e =30 μm, ρ = 0.917 g cm^{-3} sz = gamma		
	m_{ext}	ω	g	m_{ext}	ω	g	m_{ext}	ω	g	m_{ext}	ω	g
8.0	57	0.13	0.74	420	0.06	0.22	218	0.76	0.90	63	0.54	0.94
9.0	281	0.3	0.48	374	0.13	0.22	201	0.74	0.91	64	0.56	0.93
10.0	307	0.33	0.44	225	0.2	0.24	159	0.67	0.92	64	0.57	0.95
11.0	248	0.47	0.49	211	0.11	0.19	115	0.43	0.93	57	0.48	0.96
12.0	163	0.64	0.53	94	0.22	0.21	124	0.36	0.91	61	0.50	0.93
13.0	116	0.65	0.55	72	0.16	0.17	145	0.39	0.89	63	0.51	0.91

Notes: m_{ext} – [m^3 (km g)$^{-1}$], sz – size distribution, σ – standard deviation.

Table 2. Aerosol mixtures.

Mixture	Note
Andesite particles	100% andesite particle content
Water droplets	100% water droplet content
Ice crystals	100% ice crystal content
Sulfate aerosol droplets	100% SA droplet content
Andesite particles + Water droplets	Various mixtures of andesite particles with water droplets (r_e = 5,15 μm)
Andesite particles + Ice crystals	Various mixtures of andesite particles with ice crystals (r_e = 30 μm)
Sulfate aerosol droplets + Andesite particles	Various mixtures of sulfate aerosol droplets with andesite particles (r_e =1,3,5 μm)
Sulfate aerosol droplets + Water droplets	Various mixtures of sulfate aerosol droplets with water droplets (r_e = 10 μm)

and sulfate aerosol droplets, and sulfate aerosol droplets (75% H_2SO_4 and 25% H_2O), and water drops. Table 2 presents the aerosol mixtures that were used in this study.

The number of aerosol mixtures presented in Table 2 is not exhaustive, and many different variations of mixtures may occur. In this paper, only a small number of variations and two-component mixtures were considered.

Figure 2 shows r_e vs. β_{theo} for several optical models of volcanic clouds, where the numbers on the graphs show the r_e value. The dependences were plotted for aerosol particles with the following r_e ranges: 5–20 μm for water drops, 20–90 μm for ice crystals, 0.5–9 μm for andesite particles, and 0.3–3 μm for sulfate aerosol droplets. Figure 2b shows that for aerosol mixtures containing SA, there are relatively small (0.4 to 1.2) variations in $\beta_{\text{theo},12/11}$, which do not allow the aerosol mixture to be determined with certainty as the optical properties of sulfate aerosol droplets and andesite particles in the 11–12 μm atmospheric window are similar, especially for small particles (~2 μm or less). However, $\beta_{\text{theo},12/11}$ is suitable for explicitly detecting volcanic ash against a background of cloudiness. As shown, the dependences of r_e on $\beta_{\text{theo},12/11}$ for cloud and ash particles do not intersect. However, when ash particles are mixed with sulfate aerosol droplets, as is commonly the case for fresh plumes, serious difficulties may occur in detecting ash and retrieving its parameters if pure-ash-only optical models are used. The same is also true for cases in which the eruption is accompanied by the release of large amounts of a vapor–gas mixture into the atmosphere with a small amount of ash or when the ash is mixed with clouds.

In contrast, $\beta_{\text{theo},8.5/11}$ has a wider variation range (Fig. 2a) for aerosol mixtures (from 0.7 to 2.5); thus, using ratio reduces the uncertainty for the correct determination of the optical model. The coefficient $\beta_{\text{theo},8.5/11}$ makes it possible to determine the optical models of SA and its mixtures with water drops. The experiments also revealed that the values of $\beta_{\text{theo},8.5/11}$ for mixtures of andesite particles and sulfate aerosol droplets range from 1.0 to 2.5. Thus, two coefficients, $\beta_{\text{theo},8.5/11}$ and $\beta_{\text{theo},12/11}$, are the minimal requirement to select the correct optical model.

Using the single-scatter properties from the optical model, one can calculate β_{theo} and determine the SA parameters from the satellite measurements. The minimization of the sum of the residual χ^2 between the measured β_{eff} and calculated β_{theo} is used to select the optical model with the following expression:

$$\chi^2 = \frac{(\beta_{\text{eff},12/11} - \beta_{\text{theo},12/11})^2}{\beta_{\text{theo},12/11}} + \frac{(\beta_{\text{eff},8.5/11} - \beta_{\text{theo},8.5/11})^2}{\beta_{\text{theo},8.5/11}} . \quad (7)$$

Using Eq. (7), the optimal optical model is selected. The selected optical model includes an m_{ext} coefficient, which, together with the optical thickness calculated by Eq. (2), is used to calculate the aerosol mass loading M_{aer} by the following formula (Pilat and Ensor, 1971):

$$M_{\text{aer}} = \frac{\tau_{\text{aer}}}{m_{\text{ext}}} . \quad (8)$$

Thus, the coefficient β_{eff} is necessary for choosing the optical model, and calculating the aerosol mass loading by using the optical thickness. Details concerning the retrieval of these parameters will be discussed in sections 4 and 5.

3. Gaseous components of volcanic clouds

The use of three channels, 8.5, 11, and 12 μm, as described previously, is necessary to achieve a required description of the optical characteristics of aerosol components in volcanic clouds. However, when retrieving the optical parameters of an aerosol using spectral channels in the 8–13 μm wavelength range, one must consider the attenuation of electromagnetic radiation by small gaseous components of the atmosphere.

When retrieving the parameters of SA, there are also spectral absorption lines of gases such as ozone (O_3), water vapor (H_2O), and SO_2 in the 8–13 μm wavelength region, which can affect the signal registered by the satellite instrument. Ozone and water vapor in the atmosphere have low temporal variability, and their concentrations can be easily estimated using numerical weather forecast models. Among all gaseous components, SO_2 is one of the most powerful absorbers of infrared radiation. The interpretation of the atmo-

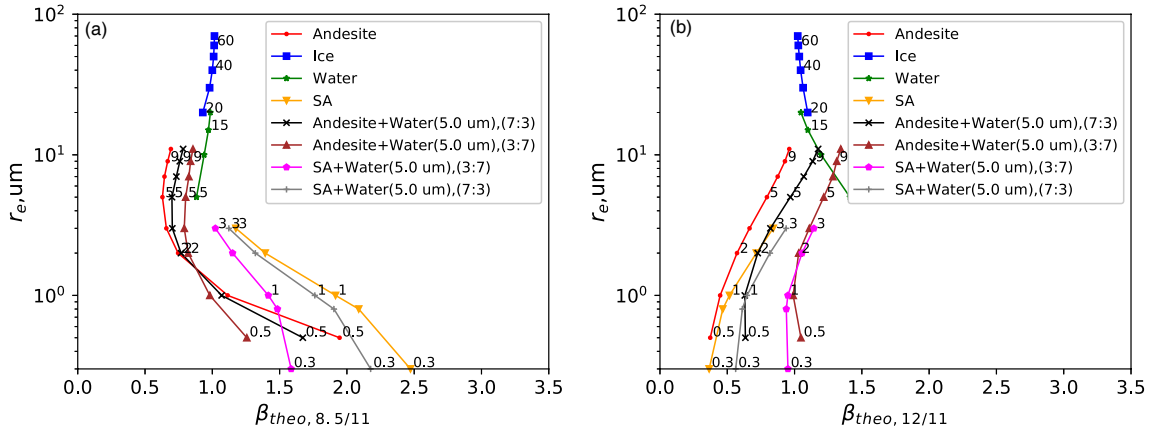

Fig. 2. Dependences of r_e on (a) $\beta_{\text{theo},8.5/11}$ and (b) $\beta_{\text{theo},12/11}$ for volcanic cloud components.

spheric concentration of SO_2 based on AHI data is complex because, in the first days after the volcanic eruption, the extinction of IR radiation at a wavelength of 8.5 μm by SO_2 molecules is many times greater than the extinction by SA particles. However, as SO_2 is degassed and turns into SA, it becomes possible to determine the sulfuric aerosol content. For example, (Guermazi et al., 2017) noted that on the 10th day after the eruption, the extinction of SA can be 40 times greater than that recorded on the first day. The eruption type plays a significant role in this process: if an eruption has high water content, SO_2 will rapidly turn into sulfuric aerosol. Infrared hyperspectrometers, such as IASI (MetOp series satellites), or UV radiometers, such as TROPOMI (Sentinel-5P), are used to consider the influence of SO_2. Given the significant effect of SO_2 on the signal recorded by the satellite instrument in the 8.5 μm wavelength region, the uncertainty in estimating the mass loading of SA can reach 35% (Guermazi et al., 2017). Moreover, the error in determining the mass loading can also reach 35%. In practice, when retrieving SO_2 or SA, it is always necessary to consider the influence of the other component.

Figure 3 presents the dependences of the differences in 8.5 and 11 μm ($BTD_{8.5\text{-}11}$) and 11 and 12 μm ($BTD_{11\text{-}12}$) brightness temperatures on the 11 μm brightness temperature (BT_{11}) for several aerosol component layer distribution scenarios of a volcanic cloud in the atmosphere.

The dependencies in Fig. 3 were obtained using the fast radiative transfer model based on the DISORT (Discrete Ordinates Radiative Transfer) code (Buras et al., 2011), which is a part of libRadtran, and the ARTS (Atmospheric Radiative Transfer Simulator) radiative transfer model www.radiative-transfer.org; Eriksson et al., 2011). The DISORT code is based on the discrete ordinate method for solving the radiative transfer equation in a plane-parallel atmosphere (Stamnes et al., 1988). The libRadtran library allows for the spectral and angular characteristics of electromagnetic radiation to be calculated based on the main optical properties of the underlying surface, the atmosphere, and its aerosol composition. The ARTS radiative transfer model (RTM) specializes in modeling IR and microwave radiation and computes atmospheric transmission via a line-by-line method along the observation path. In the present study, the ARTS RTM was used to consider the extinction of radiation by SO_2 molecules when simulating radiation in the AHI channels. The HITRAN 2012 (https://lweb.cfa.harvard.edu/HITRAN/HITRAN2012/) spectroscopic database was used for the line-by-line calculations. Figure 3 shows the most probable scenarios for the presence of volcanic cloud components in the atmosphere. The following scenarios were considered: water droplets only, water droplets and SO_2, SA only, SA and SO_2, volcanic ash only, and volcanic ash and SO_2. In all cases, the SO_2 layer with a total concentration of 100 DU was situated at an altitude of 8 km, and all other aerosol components were located at 4 km. The numbers on the graphs indicate the optical thicknesses. The simulation results presented in Fig. 3 clearly highlight the impossibility of explicitly separating the contributions of SO_2 and other volcanic cloud components. As shown, the spectral curves in Fig. 3a for SO_2-containing mixtures intersect. This can potentially lead to high uncertainty when selecting an optical model, which, in turn, will affect the accuracy of SA parameter retrieval. The difficulty in estimating the contribution of SO_2 to the resulting signal registered by the satellite instrument has been previously observed by (Sellitto and Legras, 2016; Guermazi et al., 2017). To address this issue, satellite instruments with a high spectral resolution should be used for this analysis, such as IASI (MetOp) or AIRS (Aqua), or a UV radiometer, such as TROPOMI.

Considering the uncertainty in the retrieval of SA parameters, the potential influence of other aerosols on the signal recorded by the satellite instrument should also be considered. For example, sand, dust, or smoke aerosol may have similar complex refractive indices to those of volcanic ash. Using only IR channels does not allow the contribution of these aerosols to be distinguished from volcanic components. The lower the concentration of non-volcanic aerosol

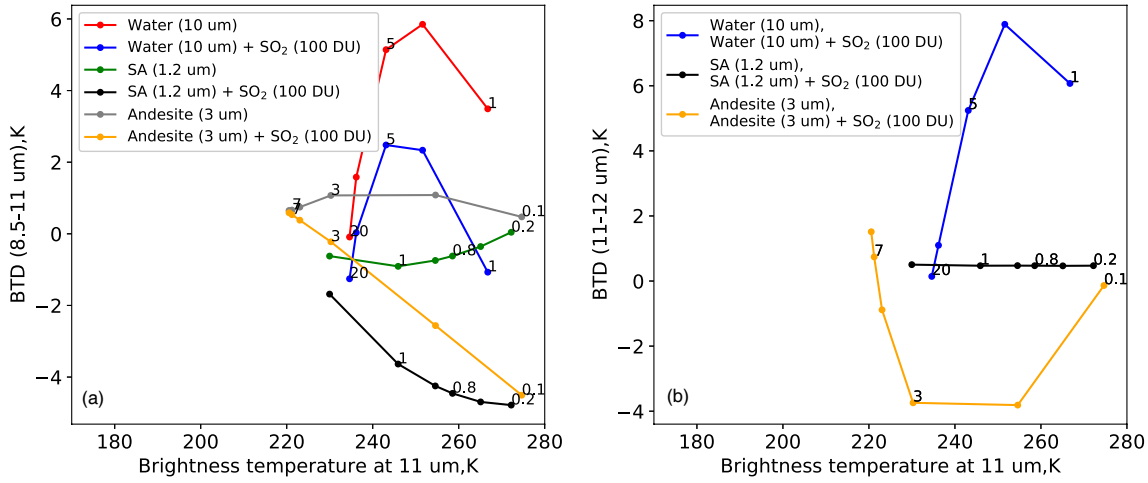

Fig. 3. Dependences of brightness temperatures in the AHI channels for several scenarios of the distribution of layers of aerosol components of a volcanic cloud in the atmosphere: (a) $BTD_{8.5\text{-}11}$ vs. BT_{11}; (b) $BTD_{11\text{-}12}$ vs. BT_{11}.

components in the atmosphere, the more difficult it is to distinguish them from volcanic ash. This problem can be partly solved by analyzing solar radiation in the visible electromagnetic spectrum in the 0.65 and 3.7 μm channels (Pavolonis et al., 2006); however, this aspect remains a subject for further research.

4. SA parameter retrieval procedure

The calculation of the SA aerosol parameters begins with detecting SA aerosol pixels in the AHI images. For detection, specially selected brightness temperature thresholds were used at wavelengths of 8.7, 11.2, and 12.4 μm, which were taken from (Ackerman and Strabala, 1994; Ackerman, 1997). For each detected pixel of the AHI image, the parameters R_{clr}, R_{ac}, and t_{ac} are determined using RTTOV (https://www.nwpsaf.eu/site/software/rttov/) (Saunders et al., 2018) calculations, which are used to determine the coefficients $\beta_{eff,8.5/11}$ and $\beta_{eff,12/11}$ using Eq. (3). Direct determination of β_{eff} is carried out by the optimal estimation method, a procedure to be discussed in detail in section 5. For RTTOV calculations, information about the state of the atmosphere and the underlying surface is required, which is taken from the GFS (Global Forecast System, https://nomads.ncep.noaa.gov) model with a spatial resolution of 0.25°. The calculations consider the spectral response function (SRF) bands of the AHI instrument. The H_2O and O_3 concentration data are taken from the GFS. The total concentration of volcanic SO_2 in the atmospheric column was calculated using the method presented in (Prata and Bernardo, 2007) by using AIRS measurements for the time point closest to that of the AHI observation. Having calculated the coefficients $\beta_{eff,8.5/11}$ and $\beta_{eff,12/11}$ for each image pixel, an optical model is selected, and the aerosol parameters are calculated. Figure 4 shows the flowchart representing the SA aerosol parameters retrieval pipeline. Details concerning the retrieval of the SA aerosol parameters are discussed in the next section.

5. Optimal estimation retrieval method

The retrieval methodology of aerosol parameters is based on an estimate of the coefficients β_{eff} and ε. The first coefficient is responsible for the choice of the optical model and m_{ext} extraction. The second coefficient is responsible for the calculation of τ_{aer}. Parameters m_{ext} and τ_{aer} are required for the calculation of aerosol mass loading.

The retrieval methodology in this study is the solution of the IR radiation transfer inverse problem. This inverse problem was solved using the optimal estimation method, which is a widely used approach in remote sensing problems that allows several interdependent target parameters to be assessed from multiple satellite instrument measurements. A detailed description of the methods for solving inverse problems involving atmospheric parameters can be found in (Rodgers, 2000; Doicu et al., 2010; Xu et al., 2016).

The retrieval procedure begins by constructing a direct model with the following form:

$$\begin{aligned}
&\mathbf{y} = \mathbf{F}(\mathbf{x}, \mathbf{p}) + \mathbf{e}\,,\\
&\mathbf{y} = [T_{11}, \mathrm{BTD}_{11,12}, \mathrm{BTD}_{11,8.5}]\,,\\
&\mathbf{x} = [\varepsilon_{11.0}, \beta_{12/11}, \beta_{8.5/11}]\,,\\
&\mathbf{p} = [R_{ac}, t_{ac}, R_{clr}, \theta, \theta_0, \varphi, \varphi_0]\,,
\end{aligned} \tag{9}$$

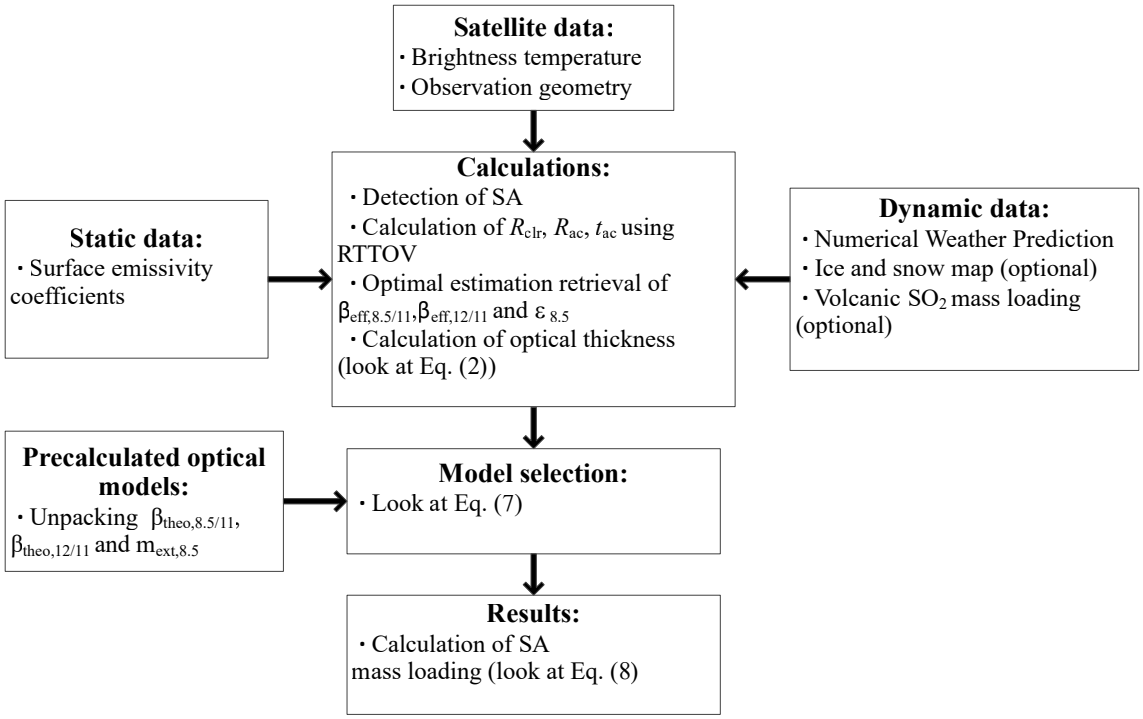

Fig. 4. Flowchart of retrieval of the SA parameters.

where **y** is the vector of measurements, **x** is the vector of required parameters, **F** is the direct model operator, **e** is measurement error, **p** is the auxiliary data vector, θ_0 is the solar zenith angle, φ is the satellite azimuth angle, φ_0 is the solar azimuth angle, and BTD is the difference in brightness temperatures.

The inverse problem must be solved to estimate the required parameters of the vector **x**, which corresponds to the case where the simulated measurements most accurately represent the actual measurements in the satellite instrument channels, taking into account measurement errors. To achieve this, the direct model given by Eq. (9) can be linearized using the following expression:

$$\begin{aligned} &\mathbf{y}-\mathbf{F}(\mathbf{x}_a,\mathbf{p}) = \mathcal{K}(\mathbf{x}-\mathbf{x}_a)+\mathbf{e}\,,\\ &\mathbf{x}_a = [\epsilon_{11.0,\mathrm{ap}},\beta_{12/11,\mathrm{ap}},\beta_{8.5/11,\mathrm{ap}}]\,,\\ &\mathcal{K} = \frac{\partial \mathbf{F}(x)}{\partial x}\,. \end{aligned} \tag{10}$$

where $\mathcal{K}$ is the matrix of weight functions (Jacobians), $\mathbf{x}_a$ is the vector of a priori information of the required parameters, and e represents the measurement errors.

The best estimate of the vector **x**, i.e., where the misfit between simulated and measured values is minimized, is determined by minimizing the objective function of the following form:

$$\phi = (\mathbf{x}-\mathbf{x}_a)^{\mathrm{T}}\mathbf{S}_a^{-1}(\mathbf{x}-\mathbf{x}_a)+(\mathbf{y}-\mathbf{F}(\mathbf{x},\mathbf{p}))^{\mathrm{T}}\mathbf{S}_y^{-1}(\mathbf{y}-\mathbf{F}(\mathbf{x},\mathbf{p}))\,, \tag{11}$$

where $\mathbf{S}_a$ is the covariance matrix of errors from the initial approximations, $\mathbf{S}_y$ is the covariance matrix of measurement errors, and ϕ is the objective function.

The parameter estimation results depend directly on a priori values and related uncertainties. The accuracy of parameter estimation of vector **x** depends on correctly constructing vector $\mathbf{x_a}$ and the covariance matrices of errors. The spectrum of particle sizes of the aerosol particle components in the volcanic cloud and the corresponding spectrum of optical thickness vary as both are controlled by the character of the volcanic explosion. Here, a priori values of $\beta_{12/11,\mathrm{ap}}$ equal to 1.1 and $\beta_{8.5/11,\mathrm{ap}}$ equal to 2.5 (the maximum values of β_{theo} presented in Fig. 2) were selected for SA. A priori values for $\varepsilon_{11,\mathrm{ap}}$ were calculated directly from satellite measurements and RTTOV simulations using Eq. (2). Since volcanic clouds may comprise different aerosol mixtures, the uncertainty in estimating a priori values of β_{theo} can be quite high, potentially reaching 100% or more of the estimated values. According to the theoretical calculations of the coefficients β_{theo} for various aerosol mixtures, some of which are presented in Fig. 2, the standard deviation σ_{ap} of the coefficient $\beta_{8.5/11,\mathrm{ap}}$ is equal to 0.4, and $\beta_{12/11,\mathrm{ap}}$ is equal to 0.2. The a priori values of the retrieved parameters and associated uncertainty estimates are shown in Table 3.

The solution to the inverse problem also requires estimation of the covariance matrix $\mathbf{S}_y$, which is based on the following error sources: radiative transfer modeling error (σ_{rtm}), instrumental noise in satellite sensor channels (σ_{instr}), calibration error (σ_{cal}), and error associated with the spatial inhomogeneity of the volcanic cloud (σ_{het}). Here, each error source is considered in detail in terms of its contribution to the resulting error.

(1) Errors in simulations with the RTTOV fast radiative transfer model: According to (Walther and Heidinger, 2012), uncertainty in the simulations can reach 5%. These errors are primarily associated with NWP errors, errors in the optical models of volume scattering of volcanic cloud particles, and errors in the RTM.

(2) Instrumental noise and IR channel calibration error: The least significant error is due to instrumental noise, whose value is constant, while calibration of the instrument channels causes the greatest error.

(3) Spatial inhomogeneity of volcanic clouds: When a pixel area in the satellite image is partly covered by clouds, this reduced cloud proportion will lead to decreased brightness temperatures in the IR channels. This reduction will be greatest for optically dense volcanic clouds with small geometric sizes. In the present study, σ_{het} was calculated for a 3 × 3 satellite image pixel block to cover pixels completely covered with clouds.

The estimation of uncertainty of the direct model for the AHI instrument is presented in Table 4.

The covariance matrix $\mathbf{S}_y$ is assumed to be diagonal and has the following form:

$$\begin{aligned} &\mathbf{S}_y = \begin{pmatrix} \sigma^2(\mathrm{BT}_{11}) & 0 & 0\\ 0 & \sigma^2(\mathrm{BTD}_{11,12}) & 0\\ 0 & 0 & \sigma^2(\mathrm{BTD}_{11,8.5}) \end{pmatrix},\\ &\sigma^2 = \sigma^2_{\mathrm{instr}}+\sigma^2_{\mathrm{het}}+\sigma^2_{\mathrm{cal}}+\sigma^2_{\mathrm{rtm}}\,, \end{aligned} \tag{12}$$

Thus, the overall uncertainty of the retrieved volcanic

Table 3. First guess values and associated uncertainties of the retrieved parameters.

Parameter	x_a	σ_{ap}
ε_{11}	$1-e^{-\frac{1}{\cos(\theta)}}$	1.0
$\beta_{8.5/11}$	2.5	0.4
$\beta_{12/11}$	1.1	0.2

Table 4. Direct model uncertainties.

Parameter	σ_{instr}	σ_{het}	σ_{clr} (water, land)	σ_{rtm}
BT_{11}	0.25 K	Calculated from actual measurements in the 3 × 3 window	0.5 K, 5.0 K	0.5 K
$\mathrm{BTD}_{11,12}$	0.25 K		0.5 K, 1.0 K	0.5 K
$\mathrm{BTD}_{8.5,11}$	0.25 K		0.5 K, 1.0 K	0.5 K

aerosol parameters will depend on the uncertainties of the a priori values (see Table 3) and the direct model (see Table 4).

For each pixel of the satellite image, the parameters ε_{11}, $\beta_{\text{eff},8.5/11}$, and $\beta_{\text{eff},12/11}$ are estimated by solving the inverse problem. Then, using Eq. (7), a suitable optical model is determined; based on this model, the effective radius of sulfate aerosol droplets, their percentage in the aerosol mixture, and m_{ext} at a wavelength of 8.5 μm are calculated. Having calculated the optical thickness τ_{aer} at a wavelength of 8.5 μm using Eq. (8), the mass loading of sulfate aerosol droplets can be represented in the following form:

$$M_{\text{aer},H_2SO_4} = \frac{P\,\tau_{\text{aer}}}{100\,m_{\text{ext}}}, \tag{13}$$

where P is the percentage of sulfate aerosol droplets in the aerosol mixture.

6. Results and discussion

The Himawari-8/AHI data were used in the above-described process to retrieve the parameters of sulfate aerosol droplets. The AHI satellite sensor has 16 spectral channels in the range of 0.45–13.3 μm with a spatial resolution of 500 m to 2 km and provides measurements with a 10-minute interval. The calibrated Himawari-8 data were taken from HimawariCloud (www.data.jma.go.jp). The study object was the eruption of the Karymsky volcano in Kamchatka, Russia, which occurred on 3 November 2021. Separate 10-minute data records from the AHI radiometer were considered using the developed methodology.

Karymsky is one of the most active volcanoes in Kamchatka. Its rocks are andesitic, and it is characterized by various eruption types. These include strombolian and vulcanian explosive eruptions with ash ejection up to 15 km above sea level (a.s.l.), effusive eruptions with extrusion of lava flows onto the volcano slopes, and extrusive eruptions with a lava dome formation in the volcano's crater (http://www.kscnet.ru/ivs/kvert/volc.php?name=Karymsky&lang=en). The volcano's activity is temporally inhomogeneous: for example, in September and October 2021, ten and seven explosions were observed, respectively. The explosions ejected ash up to 4 km a.s.l. (http://www.kscnet.ru/ivs/kvert/van/index?name=Karymsky).

On 3 November 2021 at 0720 UTC, the explosions sent ash up to 5 km a.s.l.; however, by 0748 UTC, the large ash cloud had reached 11 km a.s.l. and continued moving to the east-southeast of the volcano. The cloud remained at the same altitude (11 km a.s.l.) at 1005 UTC and then began to descend gradually. The authors assume that this large explosion was associated with the destruction of the lava dome in the volcano crater, which is consistent with the extensive release of SO_2 in this event. The strength of the explosive event on 3 November is also demonstrated by the detection of the ash cloud in Himawari-8 satellite images at a distance of >2700 km from the volcano until 6 November.

At 1550 UTC on 3 November, the eruptive cloud, which had a size of 420 × 220 km, was situated at an altitude of ~5 km a.s.l. around 400 km from the volcano (Fig. 5). The color composite presented in Fig. 5c allows the visual identification of sulfuric aerosol in the satellite image (shown in dark blue). As shown, the SA/SO_2 cloud is clearly separated from the major eruptive cloud. The difference in brightness temperature between the AIRS radiometer 1361 and 1433 cm^{-1} bands presented in Fig. 5a allows zones with high SO_2 concentrations to be identified in satellite images. The AIRS measurements were taken from (airsl1.gesdisc.eosdis.nasa.gov), and the total concentration of volcanic SO_2 in the atmospheric column was calculated using the method presented in (Prata and Bernardo, 2007) (Fig. 5b). As shown, the peak SO_2 content exceeds 100 DU, which may lead to a change in the signal in the AHI 8.5 μm channel of 4 K (Fig. 3a).

The negative and weakly positive values of the brightness temperature difference between the Himawari-8/AHI 11- and 12-μm channels shown in Fig. 5d indicate the presence of ash particles and water drops in the volcanic cloud. For the part of the volcanic cloud with a high concentration of SO_2, sulfate aerosol droplets are more likely than water droplets. The region with increased SO_2 content (~50 °–56° N, 158 °–164° W) corresponds to an elongated peak in the scatterplot of the measured $\beta_{\text{eff},8.5/11}$ and $\beta_{\text{eff},12/11}$ values as measured by the AHI (Fig. 6).

In Fig. 6, the areas related to different aerosol components (droplet clouds, ash clouds, and sulfuric clouds) can be clearly distinguished. The values of the measured coefficients β_{eff} correlate strongly with the simulated β_{theo} values presented in Fig. 2. The volcanic cloud (light blue color in Fig. 5c) has spectral characteristics closer to those of mixtures of andesite particles and water (or SA) droplets ($\beta_{\text{theo},12/11}$ = 0.75–1.1, $\beta_{\text{theo},8.5/11}$ = 0.8–1.4). The prevalence of large sulfate aerosol droplets in the cloud may indicate that the Karymsky eruption was accompanied by the release of a voluminous vapor–gas mixture into the atmosphere. This would lead to the mixing of sulfate aerosol droplets with water drops to form a low-concentration sulfur solution whose spectral characteristics are close to those of water drops.

The calculation of $\beta_{\text{theo},12/11}$ using Eq. (6), in addition to the background atmospheric transmission, also considered atmospheric transmission by volcanic SO_2 molecules, the concentration of which was computed from the AIRS data. This approach makes it possible to select a suitable optical model of a volcanic cloud and to retrieve its parameters more accurately.

Figure 7 presents the examples of SA parameters retrieved from the AHI data for the case shown in Fig. 5. To detect SA against the background of other aerosol components or the background of a clear sky, simple thresholds were used: $\beta_{\text{theo},8.5/11}$ >1.1 and $BTD_{8.5\text{-}11}$>–4. Unfortunately, when using these two thresholds, the fine droplet clouds, arctic polar aerosols, and sand and dust aerosols can also be flagged as areas containing SA. To correctly detect SA aerosol, the full range of AHI radiometer channels should

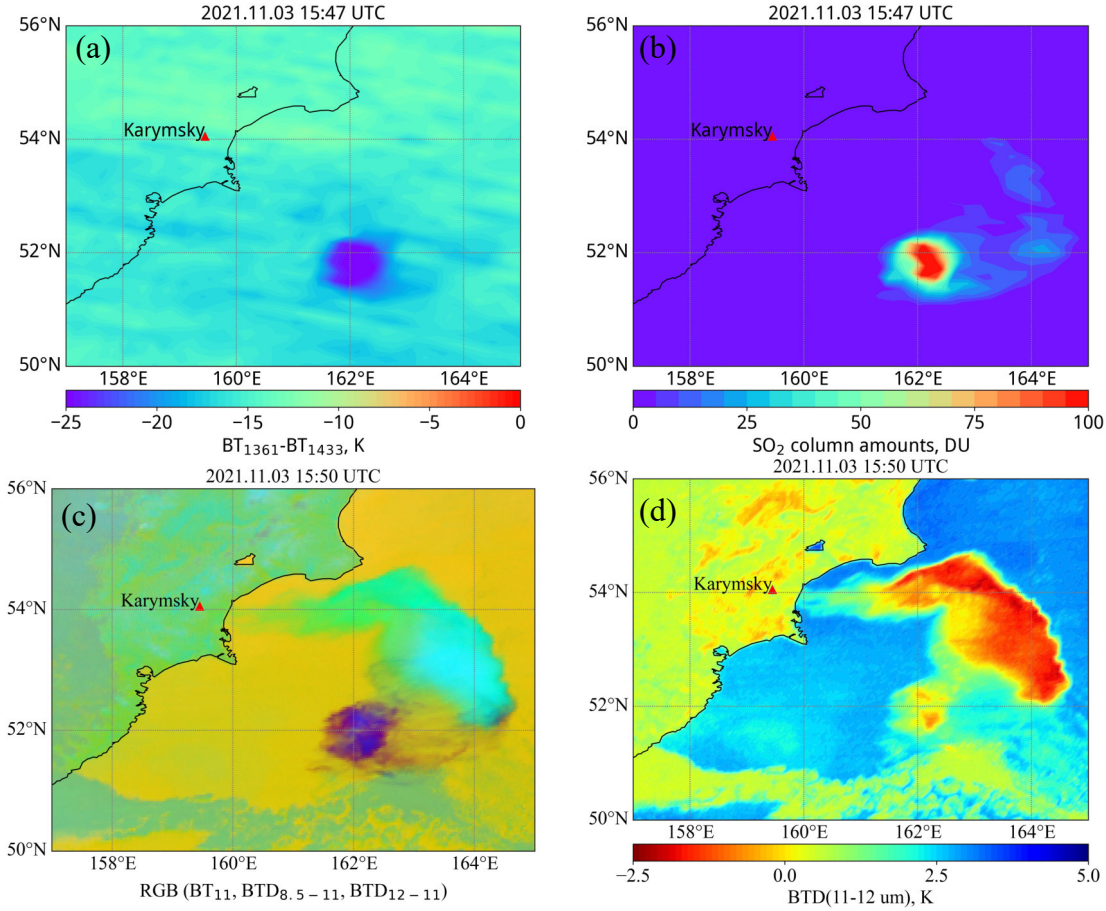

Fig. 5. The eruptive cloud of Karymsky volcano as shown in satellite data: (a) difference in the brightness temperature between the Aqua/AIRS 1361 and 1433 cm^{-1} bands, (b) mass loading of SO_2 in the atmosphere, (c) Himawari-8/AHI inverted RGB image (BT_{11}, $BTD_{8.5\text{-}11}$, $BTD_{12\text{-}11}$), and (d) the difference in brightness temperature between the Himawari-8/AHI 11 and 12 μm bands.

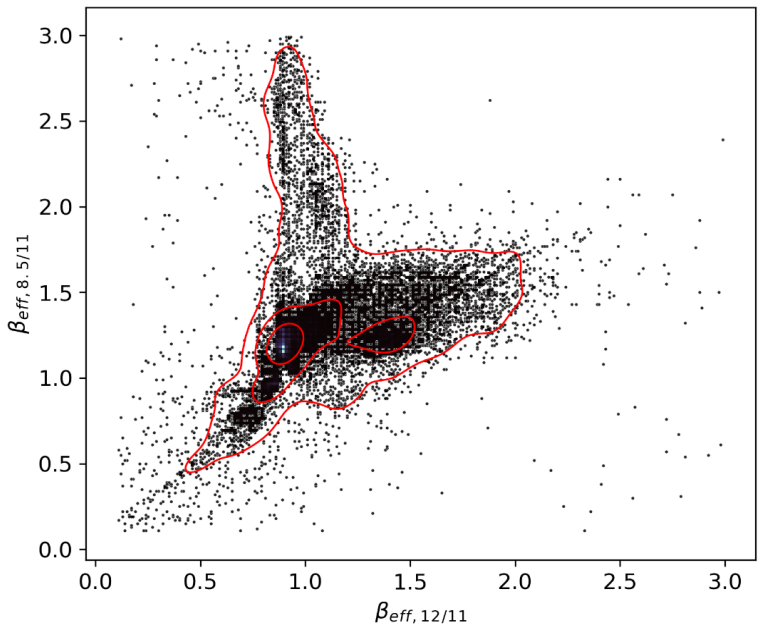

Fig. 6. Scatter plot of the measured coefficients $\beta_{eff,8.5/11}$ and $\beta_{eff,12/11}$.

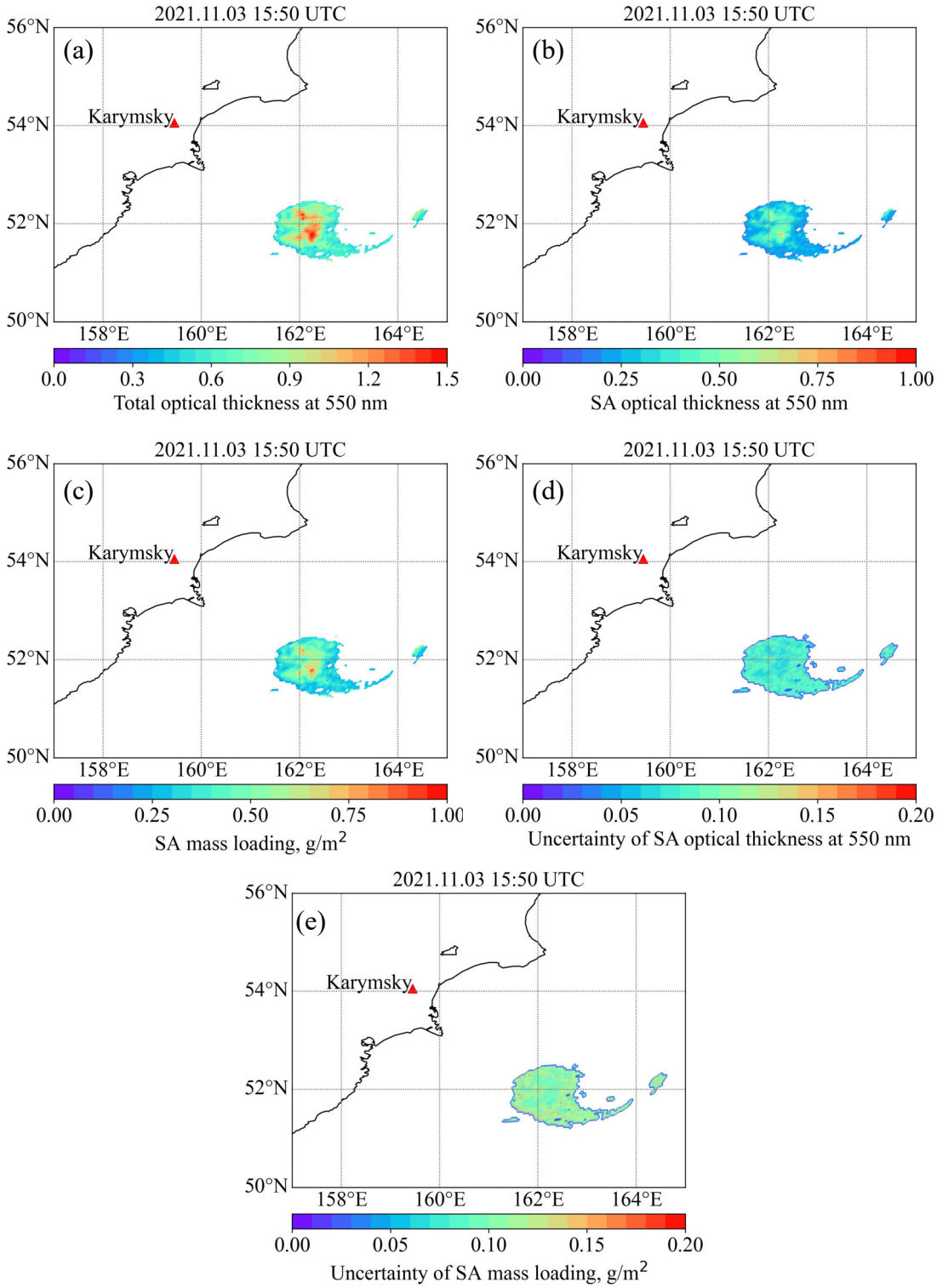

Fig. 7. The parameters of the volcanic aerosol: (a) the total optical thickness of volcanic aerosol at the wavelength of 550 nm, (b) the optical thickness of SA at a wavelength of 550 nm, (c) SA mass loading, (d) uncertainty of SA optical thickness at 550 nm, and (e) uncertainty of SA mass loading.

be used rather than only the 8.5, 11, and 12 μm channels (Ackerman et al., 2008).

The use of optical models for different volcanic aerosol component mixtures allows for the contribution of each component to the final estimate of optical parameters to be assessed. For example, Fig. 7 shows that the total optical thickness of aerosol ($\tau_{\text{aer, total}}$) (Fig. 7a) differs from the optical thickness of SA ($\tau_{\text{aer, SA}}$) (Fig. 7b), indicating that the SA is a mixture of different aerosol components. Accordingly, the mass loading of SA in the sulfuric acid cloud presented in

Fig. 7c can be evaluated. If the volcanic cloud is not considered as a mixture of different components (i.e., only pure-ash or pure-SA optical models are used), the retrieved values of the mass loading and optical thickness will contain significant errors. The uncertainties in retrieving the optical thickness and mass loading of SA aerosol are shown in Figs. 7d and 7e, respectively.

To estimate the optical properties of the sulfuric cloud,

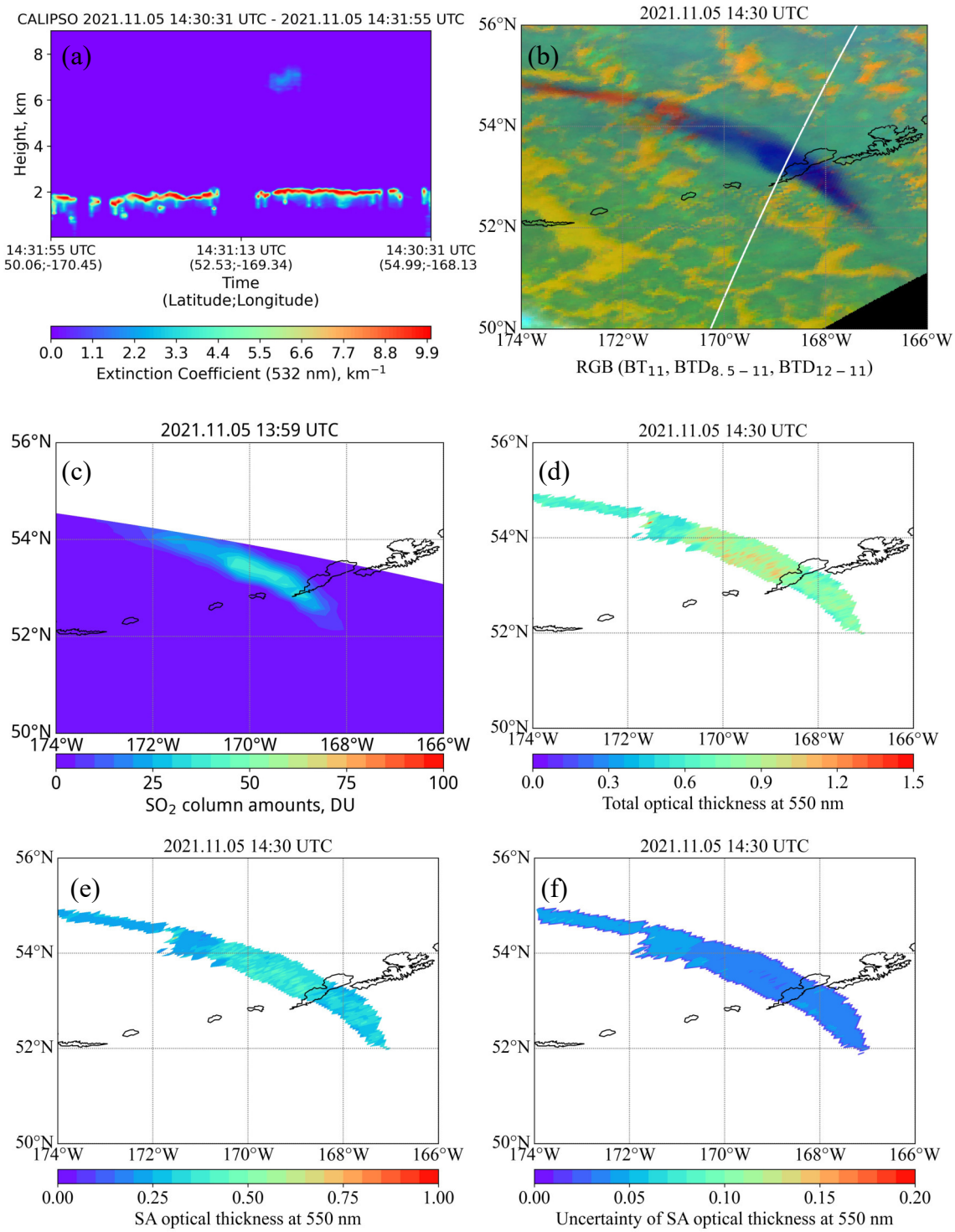

Fig. 8. Volcanic aerosol properties: (a) the extinction coefficient at a wavelength of 532 nm according to the CALIOP lidar, (b) Himawari-8/AHI inverted RGB image (BT_{11}, $BTD_{8.5\text{-}11}$, $BTD_{12\text{-}11}$) with the CALIOP trajectory (white line), (c) mass loading of SO_2 in the atmosphere, (d) the total optical thickness of volcanic aerosol at a wavelength of 550 nm, (e) the optical thickness of SA at a wavelength of 550 nm, and (e) uncertainty of SA optical thickness at 550 nm.

Fig. 8a presents the extinction coefficient at a wavelength of 532 nm (k_{532}) according to CALIPSO/CALIOP lidar data (ftp.icare.univ-lille1.fr). Additionally, Figs. 8b and 8c present a Himawari-8/AHI inverted RGB image indicating the trajectory of the CALIOP lidar (white line) and mass loading of SO_2 in the atmosphere, respectively. The total optical thickness of volcanic aerosol at a wavelength of 550 nm is presented in Fig. 8d. The SA optical thickness and its uncertainty are presented in Fig. 8e and Fig. 8f, respectively.

The trajectories of the CALIPSO satellite and the sulfuric cloud only intersected at 1430 UTC on 5 November 2021. Based on the coordinates at this time, the sulfuric cloud (Fig. 8b) was located >2000 km from the Karymsky volcano at an altitude of 7 km, with an average thickness of ~800 m. The optical thickness of the sulfuric cloud was an order of magnitude lower than the optical thickness of the stratiform cloudiness at the time, which was situated at an altitude of 2 km (Fig. 8a).

Having integrated k_{532} over altitude in the atmospheric layer from the base (~6.5 km) to the top (~7.5 km) of the sulfuric cloud, the average total optical thickness of sulfuric acid aerosol was estimated based on the CALIOP data and found to be equal to ~0.95 (maximum of ~1.40). Having matched the CALIOP trajectory with the AHI data, the optical thickness according to the AHI measurements was estimated at ~0.88 (maximum of ~1.19). The optical thickness values of the sulfuric acid cloud derived from CALIOP and AHI data correlate well. The maximum values of the SA optical thickness do not exceed 45% of the total optical thickness, indicating that the optical properties of the sulfuric cloud were almost unchanged two days after the eruption. Given that the explosions lifted the eruptive cloud to an altitude of 11 km a.s.l., i.e., above the tropopause (~8 km according to the GFS numerical weather prediction model), and no other clouds were present along the volcanic cloud's path, its optical properties remained unchanged for an extended period.

The total mass of SA released into the atmosphere during the Karymsky eruption was also estimated for the case presented in Fig. 8. Taking into account the uncertainty of retrieved mass loading, and since the AHI IR pixel area is 4 km^2, the total mass of SA is at least 1775±521 tons. The uncertainty in retrieving the mass loading has an average value of 0.06 g m^{-2} and optical thickness of –0.04, with maximum values of 0.12 g m^{-2} and 0.09, respectively. Total uncertainty for column mass loading estimations was ~ 35%.

A comparison of the satellite and lidar-derived estimates of mass loading and optical thickness was performed based on the following scheme. First, for the AHI data measured at 1430 UTC on 5 November 2021, the parallax effect was corrected as the true object position and will not match the observed one when observing an object from a geostationary orbit at large zenith angle. Next, spatial alignment was performed by searching for the nearest lidar measurement to each pixel containing SA according to the AHI data. Measurements with an optical thickness of less than 0.1 indicate the absence of sulfuric acid aerosol and were thus excluded from the comparison. The shooting time between the AHI and CALIOP data did not exceed two minutes. Based on these conditions, only 11 cases were selected from the entire dataset of lidar measurements. Table 5presents the results of the total optical thickness comparison. Despite the sparse test date, the comparison of the total optical thickness results yielded a correlation coefficient of ~0.7, indicating good agreement between satellite- and lidar-derived estimates of volcanic ash parameters.

The use of independent satellite lidar measurements during the eruption of the Karymsky volcano made it possible to verify the volcanic SA parameters retrieved from satellite data. While a good correlation between satellite and lidar estimates of SA parameters was achieved, there are also several key limitations in the presented methodology.

(1) The requirement for independent SO_2 measurements, e.g., from IR hyperspectrometers, or UV radiometers: The use of these measurements allows the contribution of the attenuation of IR radiation by SO_2 molecules recorded by the AHI channels to be considered. In the absence of these data, the proposed technique should be applied when most of the SO_2 has been turned to SA via hydration. In general, this occurs five days after the eruption but ultimately depends on the nature of the volcanic eruption. The more water vapor that is present in the volcanic cloud, the faster SO_2 is transformed into sulfuric acid aerosol.

(2) Inhomogeneous structure of the volcanic cloud: Since an AHI-type satellite instrument measures radiation directly from the upper layer of the volcanic cloud, it will not be able to obtain information about the underlying layers of multilayer clouds, which can often have higher sulfuric acid aerosol particle concentrations than the cloud's upper layer. The solution to this issue is to use independent measurements of the vertical distribution of cloudiness, e.g., MW or IR measurements.

(3) Influence of the underlying surface: The algorithm was tested over the sea surface only, whose emissivity is stable in the wavelength range of 8–13 μm, irrespective of the season. However, for this method to work correctly when observing volcanic clouds from above the Earth's surface, special emissivity atlases should be used.

(4) Two-component aerosol mixtures: In reality, a volcanic cloud can consist of much more than two components. The use of multi-component mixtures will require measurements in a larger number of spectral channels, for example, in the 0.6 and 3.7 μm channels.

(5) Non-volcanic aerosols: Sand, dust, or smoke aerosol may have (8–13 μm) similar optical properties to

Table 5. Total optical thickness comparison results.

N	RMSE	MAE	ME	*R*
11	0.29	0.22	–0.18	0.76

Notes: RMSE—Root Mean Square Error, MAE—Mean Absolute Error, ME—Mean Error, *R*—Pearson correlation coefficient, *N*—Number of measurements.

those of volcanic ash in the infrared range. When using only IR channels, it is hard to distinguish between the contribution of these aerosols from other volcanic components. This problem can be partly solved by using the 0.65 and 3.7 μm channels.

(6) Sulfate aerosol of different proportions. In the presented work, a sulfate aerosol in the proportion of 75% H_2SO_4 and 25% H_2O was used to construct optical models. However, in real conditions during volcanic emissions, the proportions of SA can be different. As a result, refractive indices may change, altering the aerosol optical properties, which must be accounted for.

7. Conclusions

This paper presents a method for retrieving the optical parameters of volcanic SA from the AHI sensor on board Himawari-8. This method is based on applying optical models for different mixtures of volcanic cloud aerosol components consisting of ash particles, ice crystals, water drops, and sulfate aerosol droplets. The use of multi-component models with different combinations of aerosol fractions allowed the spectral characteristics of the volcanic cloud to be correctly estimated for the case of the Karymsky volcano eruption and the optical thickness and mass loading of SA to be retrieved. In addition, the use of these models enabled the estimation of optical parameters not only for SA but also for the whole aerosol mixture. A comparison of the optical thicknesses of the sulfuric acid aerosol derived from the AHI radiometer and CALIOP lidar data demonstrated good consistency, with the average values of $\tau_{aer,total}$ calculated as 0.88 and 0.95, respectively.

The main limitation of the presented method is its inability to accurately retrieve the optical parameters of SA from satellite instruments with broadband channels, including the AHI radiometer. Broadband channels do not allow the individual radiation contributions of SO_2 and SA to the resulting signal registered by the satellite channels to be distinguished. It is essentially impossible to use broadband satellite instrument measurements alone to independently estimate SA parameters with high precision. Accordingly, measurements from satellite instruments with high spectral resolution should be used, such as IASI, AIRS, CrIS, or measurements from UV radiometers, such as TROPOMI.

Future research should study retrieving the parameters of sulfuric acid aerosol using additional measurements from the visible wavelength range. In addition, complex volcanic eruption cases should be investigated in which volcanic clouds overlap with ordinary clouds. Cases should also be investigated involving volcanic clouds over the land, and the behavior of the algorithm should also be investigated when analyzing dust, smoke, or sand aerosols. These approaches would allow volcanologists to perform a comprehensive analysis of volcanic clouds to more precisely assess their risk to aviation.

The presented method for retrieving the SA optical parameters can be used for any satellite sensor with a combination of channels 8.5, 11, and 12 μm after considering the characteristics of their SRFs. In addition, the presented method can be potentially applied to measurements from the AGRI broadband radiometer and the GIIRS-2 infrared hyperspectral radiometer on board the Chinese geostationary satellite of the Feng Yung series (FY-4A/B). Simultaneous use of data from the AGRI and GIIRS-2 instruments could effectively address the problem of the impacts of SO_2 on the accuracy of retrieving the SA optical parameters.

Acknowledgements. The studies were carried out using the resources of the Center for Shared Use of Scientific Equipment "Center for Processing and Storage of Scientific Data of the Far Eastern Branch of the Russian Academy of Sciences" (Sorokin et al., 2017) (Project No. 075-15-2021-663).

REFERENCES

Ackerman, S. A., 1997: Remote sensing aerosols using satellite infrared observations. *J. Geophys. Res.*, **102**(D14), 17 069–17 079, https://doi.org/10.1029/96JD03066.

Ackerman, S. A., and K. I. Strabala, 1994: Satellite remote sensing of H_2SO_4 aerosol using the 8- to 12-μm window region: Application to Mount Pinatubo. *J. Geophys. Res.*, **99**(D9), 18 639–18 649, https://doi.org/10.1029/94JD01331.

Ackerman, S. A., A. J. Schreiner, T. J. Schmit, H. M. Woolf, J. Li, and M. Pavolonis, 2008: Using the GOES Sounder to monitor upper level SO_2 from volcanic eruptions. *J. Geophys. Res.*, **113**, D14S11, https://doi.org/10.1029/2007JD009622.

Baum, B. A., A. J. Heymsfield, P. Yang, and S. T. Bedka, 2005a: Bulk scattering properties for the remote sensing of ice clouds. Part I: Microphysical data and models. *J. Appl. Meteorol. Climatol.*, **44**, 1885–1895, https://doi.org/10.1175/JAM2308.1.

Baum, B. A., P. Yang, A. J. Heymsfield, S. Platnick, M. D. King, Y.-X. Hu, and S. T. Bedka, 2005b: Bulk scattering properties for the remote sensing of ice clouds. Part II: Narrowband models. *J. Appl. Meteorol. Climatol.*, **44**, 1896–1911, https://doi.org/10.1175/JAM2309.1.

Bennis, K., and E. Venzke, 2022: Report on Hunga Tonga-Hunga Ha'apai (Tonga). *Bulletin of the Global Volcanism Network*, **47**(3), 10 pp, https://doi.org/10.5479/si.GVP.BGVN202203-243040.

Bugliaro, L., and Coauthors, 2022: VADUGS: A neural network for the remote sensing of volcanic ash with MSG/SEVIRI trained with synthetic thermal satellite observations simulated with a radiative transfer model. *Natural Hazards and Earth System Sciences*, **22**(3), 1029–1054, https://doi.org/10.5194/nhess-22-1029-2022.

Buras, R., T. Dowling, and C. Emde, 2011: New secondary-scattering correction in DISORT with increased efficiency for forward scattering. *Journal of Quantitative Spectroscopy and Radiative Transfer*, **112**(12), 2028–2034, https://doi.org/10.1016/j.jqsrt.2011.03.019.

Clarisse, L., and F. Prata, 2016: Infrared sounding of volcanic ash. *Volcanic Ash: Hazard Observation*, S. Mackie, K. Cashman, H. Ricketts, A. Rust, M. Watson, Eds., Elsevier, 189–215, https://doi.org/10.1016/B978-0-08-100405-0.00017-3.

Clarisse, L., D. Hurtmans, A. J. Prata, F. Karagulian, C. Clerbaux, M. De Mazière, and P.-F. Coheur, 2010: Retrieving radius, concentration, optical depth, and mass of different types of aerosols from high-resolution infrared nadir spectra. *Appl. Opt.*, **49**(19), 3713–3722, https://doi.org/10.1364/AO.49.003713.

Doicu A., T. Trautmann, and F. Schreier, 2010: *Numerical Regularization for Atmospheric Inverse Problems*. Springer, 426 pp.

Eisinger, M., and J. P. Burrows, 1998: Tropospheric sulfur dioxide observed by the ERS-2 GOME instrument. *Geophys. Res. Lett.*, **25**(22), 4177–4180, https://doi.org/10.1029/1998GL900128.

Ensor, D. S., and M. J. Pilat, 1971: Calculation of smoke plume opacity from particulate air pollutant properties. *Journal of the Air Pollution Control Association*, **21**(8), 496–501, https://doi.org/10.1080/00022470.1971.10469561.

Eriksson, P., S. A. Buehler, C. P. Davis, C. Emde, and O. Lemke, 2011: ARTS, the atmospheric radiative transfer simulator, version 2. *Journal of Quantitative Spectroscopy and Radiative Transfer*, **112**(10), 1551–1558, https://doi.org/10.1016/j.jqsrt.2011.03.001.

Filei, A. A., and F. Marenco, 2021: Retrieval of volcanic ash parameters from satellite data. *Russian Meteorology and Hydrology*, **46**(4), 269–279, https://doi.org/10.3103/s1068373921040087.

Girina, O., S. Malkovsky, A. Sorokin, E. Loupian, and S. Korolev, 2022: Numerical modeling of the ash cloud movement from the catastrophic eruption of the Sheveluch volcano in November 1964. *Remote Sensing*, **14**, 3449, https://doi.org/10.3390/rs14143449.

Guermazi, H., P. Sellitto, M. M. Serbaji, B. Legras, and F. Rekhiss, 2017: Assessment of the combined sensitivity of Nadir TIR satellite observations to volcanic SO_2 and sulphate aerosols after a moderate stratospheric eruption. *Geosciences*, **7**(3), 84, https://doi.org/10.3390/geosciences7030084.

Hale, G. M., and M. R. Querry, 1973: Optical constants of water in the 200-nm to 200-μm wavelength region. *Appl. Opt.*, **12**(3), 555–563, https://doi.org/10.1364/ao.12.000555.

Hedelt, P., D. S. Efremenko, D. G. Loyola, R. Spurr, and L. Clarisse, 2019: Sulfur dioxide layer height retrieval from Sentinel-5 Precursor/TROPOMI using FP_ILM. *Atmospheric Measurement Techniques*, **12**, 5503–5517, https://doi.org/10.5194/amt-12-5503-2019.

Heidinger, A. K., and M. J. Pavolonis, 2009: Gazing at cirrus clouds for 25 years through a split window. Part I: Methodology. *J. Appl. Meteorol. Climatol.*, **48**, 1100–1116, https://doi.org/10.1175/2008JAMC1882.1.

Ishii, K., Y. Hayashi, and T. Shimbori, 2018: Using Himawari-8, estimation of SO_2 cloud altitude at Aso volcano eruption, on October 8, 2016. *Earth, Planets and Space*, **70**, 19, https://doi.org/10.1186/s40623-018-0793-9.

Karagulian, F., L. Clarisse, C. Clerbaux, A. J. Prata, D. Hurtmans, and P. F. Coheur, 2010: Detection of volcanic SO_2, ash, and H_2SO_4 using the Infrared Atmospheric Sounding Interferometer (IASI). *J. Geophys. Res.*, **115**, D00L02, https://doi.org/10.1029/2009JD012786.

Koukouli, M.-E., and Coauthors, 2022: Volcanic SO_2 layer height by TROPOMI/S5P: Evaluation against IASI/MetOp and CALIOP/CALIPSO observations. *Atmospheric Chemistry and Physics*, **22**, 5665–5683, https://doi.org/10.5194/acp-22-5665-2022.

Li, C., J. Joiner, F. Liu, N. A. Krotkov, V. Fioletov, and C. McLinden, 2022: A new machine-learning-based analysis for improving satellite-retrieved atmospheric composition data: OMI SO_2 as an example. *Atmospheric Measurement Techniques*, **15**, 5497–5514, https://doi.org/10.5194/amt-15-5497-2022.

Liu, X. H., and J. E. Penner, 2002: Effect of Mount Pinatubo H_2SO_4/H_2O aerosol on ice nucleation in the upper troposphere using a global chemistry and transport model. *J. Geophys. Res.*, **107**(D12), 4141, https://doi.org/10.1029/2001JD000455.

Mayer, B., and A. Kylling, 2005: Technical note: The libRadtran software package for radiative transfer calculations – description and examples of use. *Atmospheric Chemistry and Physics*, **5**, 1855–1877, https://doi.org/10.5194/acp-5-1855-2005.

McCormick, M. P., L. W. Thomason, and C. R. Trepte, 1995: Atmospheric effects of the Mt Pinatubo eruption. *Nature*, **373**(6513), 399–404, https://doi.org/10.1038/373399a0.

Miller, T. P., and T. J. Casadevall, 2000: Volcanic ash hazards to aviation. *Encyclopedia of Volcanoes*, H. Sigurdsson, Ed., Academic Press, 915–930.

Ohtake, T., 1993: Freezing points of H_2SO_4 aqueous solutions and formation of stratospheric ice clouds. *Tellus B*: *Chemical and Physical Meteorology*, **45**(2), 138–144, https://doi.org/10.3402/tellusb.v45i2.15588.

Parol, F., J. C. Buriez, G. Brogniez, and Y. Fouquart, 1991: Information content of AVHRR channels 4 and 5 with respect to the effective radius of cirrus cloud particles. *J. Appl. Meteorol.*, **30**(7), 973–984, https://doi.org/10.1175/1520-0450-30.7.973.

Pavolonis, M. J., 2010: Advances in extracting cloud composition information from spaceborne infrared radiances – A robust alternative to brightness temperatures. Part I: Theory. *J. Appl. Meteorol. Climatol.*, **49**(9), 1992–2012, https://doi.org/10.1175/2010JAMC2433.1.

Pavolonis, M. J., W. F. Feltz, A. K. Heidinger, and G. M. Gallina, 2006: A daytime complement to the reverse absorption technique for improved automated detection of volcanic ash. *J. Atmos. Oceanic Technol.*, **23**(11), 1422–1444, https://doi.org/10.1175/JTECH1926.1.

Pavolonis, M. J., A. K. Heidinger, and J. Sieglaff, 2013: Automated retrievals of volcanic ash and dust cloud properties from upwelling infrared measurements. *J. Geophys. Res.*, **118**(3), 1436–1458, https://doi.org/10.1002/jgrd.50173.

Pilat, M. J., and D. S. Ensor, 1971: Comparison between the light extinction aerosol mass concentration relationship of atmospheric and air pollutant emission aerosols. *Atmos. Environ.*, **5**(4), 209–215, https://doi.org/10.1016/0004-6981(71)90090-4.

Piontek, D., L. Bugliaro, J. Kar, U. Schumann, F. Marenco, M. Plu, and C. Voigt, 2021: The new volcanic ash satellite retrieval VACOS using MSG/SEVIRI and artificial neural networks: 2. Validation. *Remote Sensing*, **13**(16), 3128, https://doi.org/10.3390/rs13163128.

Pollack, J. B., O. B. Toon, and B. N. Khare, 1973: Optical properties of some terrestrial rocks and glasses. *Icarus*, **19**(3), 372–389, https://doi.org/10.1016/0019-1035(73)90115-2.

Prata, A. J., 1989: Observations of volcanic ash clouds in the 10-12 μm window using AVHRR/2 data. *Int. J. Remote Sens.*, **10**(4–5), 751–761, https://doi.org/10.1080/01431168908903916.

Prata, A. J., and C. Bernardo, 2007: Retrieval of volcanic SO_2 col-

umn abundance from Atmospheric Infrared Sounder data. *J. Geophys. Res.*, **112**, D20204, https://doi.org/10.1029/2006JD007955.

Prata, F., and B. Rose, 2015: Volcanic ash hazards to aviation. *Encyclopedia of Volcanoes*. 2nd ed, H. Sigurdsson, Ed., Academic Press, 911–934, https://doi.org/10.1016/B978-0-12-385938-9.00052-3.

Remsberg, E. E., D. Lavery, and B. Crawford Jr, 1974: Optical constants for sulfuric and nitric acids. *Journal of Chemical and Engineering Data*, **19**(3), 263–265, https://doi.org/10.1021/je60062a003.

Roberts, T. J., and Coauthors, 2018: The primary volcanic aerosol emission from Mt Etna: Size-resolved particles with SO_2 and role in plume reactive halogen chemistry. *Geochimica et Cosmochimica Acta*, **222**, 74–93, https://doi.org/10.1016/j.gca.2017.09.040.

Rodgers, C. D., 2000: *Inverse Methods for Atmospheric Sounding: Theory and Practice*. World Scientific, 256 pp, https://doi.org/10.1142/3171.

Saunders, R., and Coauthors, 2018: An update on the RTTOV fast radiative transfer model (currently at version 12). *Geoscientific Model Development*, **11**, 2717–2737, https://doi.org/10.5194/gmd-11-2717-2018.

Sellitto, P., and B. Legras, 2016: Sensitivity of thermal infrared nadir instruments to the chemical and microphysical properties of UTLS secondary sulfate aerosols. *Atmospheric Measurement Techniques*, **9**, 115–132, https://doi.org/10.5194/amt-9-115-2016.

Sellitto, P., G. Sèze, and B. Legras, 2017: Secondary sulphate aerosols and cirrus clouds detection with SEVIRI during Nabro volcano eruption. *Int. J. Remote Sens.*, **38**(20), 5657–5672, https://doi.org/10.1080/01431161.2017.1348635.

Sellitto, P., R. Siddans, R. Belhadji, E. Carboni, B. Legras, A. Podglajen, C. Duchamp, and B. Kerridge, 2023: Observing the SO_2 and sulphate aerosol plumes from the 2022 Hunga Tonga-Hunga Ha'apai eruption with IASI. *Geophysical Research Letters*, 12 pp, https://doi.org/10.22541/essoar.169091894.48592907/v1.

Sorokin, A. A., S. V. Makogonov, and S. P. Korolev, 2017: The information infrastructure for collective scientific work in the Far East of Russia. *Scientific and Technical Information Processing*, **44**, 302–304, https://doi.org/10.3103/S0147688217040153.

Stamnes, K., S.-C. Tsay, W. Wiscombe, and K. Jayaweera, 1988: Numerically stable algorithm for discrete-ordinate-method radiative transfer in multiple scattering and emitting layered media. *Appl. Opt.*, **27**(12), 2502–2509, https://doi.org/10.1364/AO.27.002502.

Theys, N., I. De Smedt, C. Lerot, H. Yu, and M. Van Roozendael, 2023: S5P/TROPOMI SO_2 ATBD, 75 pp. Available from https://sentinel.esa.int/documents/247904/2476257/Sentinel-5P-ATBD-SO2-TROPOMI.

Ulfarsson, G. F., and E. A. Unger, 2011: Impacts and responses of Icelandic aviation to the 2010 Eyjafjallajökull volcanic eruption: Case study. *Transportation Research Record*: *Journal of the Transportation Research Board*, **2214**(1), 144–151, https://doi.org/10.3141/2214-18.

Walther, A., and A. K. Heidinger, 2012: Implementation of the daytime cloud optical and microphysical properties algorithm (DCOMP) in PATMOS-x. *J. Appl. Meteorol. Climatol.*, **51**(7), 1371–1390, https://doi.org/10.1175/JAMC-D-11-0108.1.

Warren, S. G., 1984: Optical constants of ice from the ultraviolet to the microwave. *Appl. Opt.*, **23**, 1206–1225, https://doi.org/10.1364/AO.23.001206.

Wen, S. M., and W. I. Rose, 1994: Retrieval of sizes and total masses of particles in volcanic clouds using AVHRR bands 4 and 5. *J. Geophys. Res.*, **99**(D3), 5421–5431, https://doi.org/10.1029/93JD03340.

Xu, J., F. Schreier, A. Doicu, and T. Trautmann, 2016: Assessment of Tikhonov-Type regularization methods for solving atmospheric inverse problems. *Journal of Quantitative Spectroscopy and Radiative Transfer*, **184**, 274–286, https://doi.org/10.1016/j.jqsrt.2016.08.003.